Available online at www.sciencedirect.com
ScienceDirect
Comput. Methods Appl. Mech. Engrg. 339 (2018) 184–204
Computer methods in applied mechanics and engineering
www.elsevier.com/locate/cma

An integrated process–structure–property modeling framework for additive manufacturing

Wentao Yan[1], Yanping Lian[1], Cheng Yu[1], Orion L. Kafka[1], Zeliang Liu, Wing Kam Liu, Gregory J. Wagner*

Department of Mechanical Engineering, Northwestern University, Evanston, IL 60208, United States

Received 14 December 2017; received in revised form 6 April 2018; accepted 3 May 2018
Available online 12 May 2018

Abstract

One goal of modeling for metal Additive Manufacturing (AM) is to predict the resultant mechanical properties from given manufacturing process parameters and intrinsic material properties, thereby reducing uncertainty in the material built. This can dramatically reduce the time and cost for the development of new products using AM. We have realized the seamless linking of models for the manufacturing process, material structure formation, and mechanical response through an integrated multi-physics modeling framework. The sequentially coupled modeling framework relies on the concept that the results from each model used in the framework are contained in space-filling volume elements using a prescribed structure. This framework is implemented to show a prediction of the decrease in fatigue life caused by insufficient fusion resulting from low laser power relative to the hatch spacing. In this demonstration, powder spreading and thermal-fluid flow models are used to predict the thermal history and void formation in a multilayer, multi-track build with different processing conditions. The results of these predictions are passed to a cellular automaton-based prediction of grain structure. Finally, the predicted grain and void structure is passed to a reduced-order micromechanics-based model to predict mechanical properties and fatigue life arising from the different processing conditions used in the process model. The simulation results from this combination of models demonstrate qualitative agreement with experimental observations from literature, showing the appealing potential of an integrated framework.

Keywords: Additive manufacturing; Reduced order modeling; Process modeling; Grain growth; Process–structure–property

1. Introduction

Metal-based additive manufacturing (AM) is widely considered a promising technology, with many potential applications due to the flexibility of the process. This flexibility is achieved in part because the process is highly localized; however, these processes lack reproducibility and reliability: the quality of the parts produced is sensitive

* Corresponding author.
E-mail address: gregory.wagner@northwestern.edu (G.J. Wagner).
[1] These authors contribute equally to this work.

https://doi.org/10.1016/j.cma.2018.05.004
0045-7825/

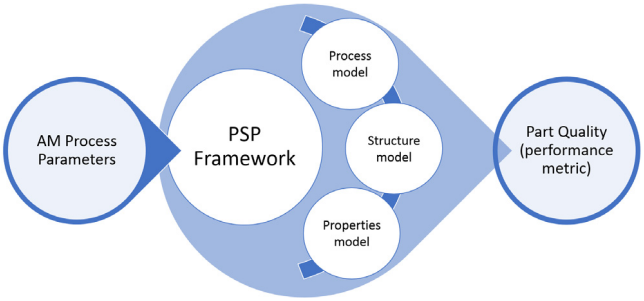

Fig. 1. The goal of the framework is to seamlessly link AM process parameters to part quality, measured by a performance metric, using predictive modeling.

to local and global build conditions. To overcome the challenges this poses in the production of functional, load-bearing or otherwise practically useful components, significant effort has been expended. Computational modeling is an appealing approach to understand the complex relationships between the processing conditions and part quality. In this paper, we will show an important advance in this field: a method and application to directly connect process modeling, through microstructural information, to material performance metrics, as schematically shown in Fig. 1. We show an example where increasing hatch spacing (decreasing power density) results in a void, which causes a reduction in the predicted fatigue life of a predicted microstructure.

Many models have been developed to understand AM from various perspectives including temperature field [1–3], molten pool flow [4–7], residual stress [8–11] and mechanical properties [12,13]. However, most models in the current literature are not connected, thereby lacking comprehensive understanding of process–structure–property relationships. Recent reviews and opinion papers, e.g. [14,15], have called for the integration of process–structure and structure–property–performance tools for predictive computational modeling to further enable AM. By providing predictive models that mimic the stages of production and use of a part, these tools could allow for higher confidence in AM parts and an integration of part and process design to maximize the potential of AM. Francois et al. [16] demonstrate a number of recent advances in modeling for process to structure, structure to properties, and properties to part performance. However, they do not propose a means of connecting these tools. Indeed, they state that such a combination would benefit the AM community. Collins et al. present a predominantly continuum scale process–structure–properties integration for a Titanium alloy [17]. Only the macroscale is considered, which may be insufficient to assess damage or failure. Moreover, no generalized structure or framework is provided, resulting in limited applicability outside of the specific simulations presented [17]. Our own recent perspectives articles, e.g. [18–20], have included statements to similar effect, and with a similar shortcoming: lack of the demonstration of a definitive framework and implementation.

The purpose of the current paper is to remedy that shortcoming by demonstrating concretely an integrated framework and describing a generalization of the framework that achieves the breadth necessary to warrant the term.

2. AM modeling framework

Here we present a process–structure–property prediction framework for metal additive manufacturing, with an implementation for selective electron beam melting (SEBM) of the commonly used Titanium alloy, Ti–6Al–4V. In this framework, shown schematically in Fig. 2, each model incorporates basic material information and data provided directly from previous models in the framework to predict the mechanical response and estimated fatigue life of critical microstructures given machine-relevant processing conditions. The key idea of the framework is that structural information, data that can be represented in space using a collection of volume-filling elements, sufficiently describes the system and can thus intermediate models: a common yet powerful premise.

In abstract form, the framework consists of various “modules” that are aggregated into “hubs;” there may be multiple hubs, each of which collects and passes a complete solution for one stage (e.g. process simulation) to the next stage (e.g. mechanical response prediction). One might think of our *modules* as discrete processing units capturing a unique facet of the system and *hubs* as data management facilities for database queries. To systematize the method we group modules into hubs for (1) material processing and (2) material response.

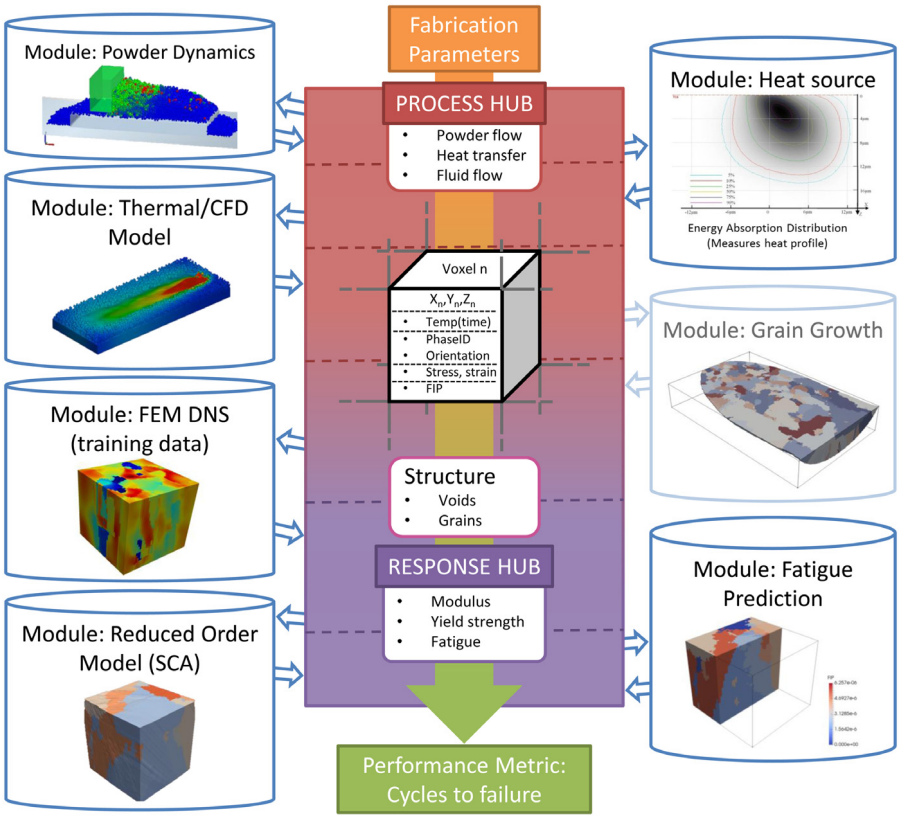

Fig. 2. Schematic diagram of the module-hub framework conceptual layout, with images of our current implementation demonstrating the modules: a SEBM process with microstructure-based fatigue life assessment. The data used by the framework at each point in space is described by spatial coordinates and any relevant field data for the current working modules, as shown graphically by a schematic of a representative voxel. The cellular automaton model is shaded gray to indicate that results both with and without it are given, to demonstrate the flexibility of the framework.

Each module is stand-alone, designed to answer significant scientific and/or engineering questions independent of the connecting framework. As such, the models that make up our modules will only be discussed with sufficient detail to elucidate their purpose: the key points of each are provided. The interested reader is directed to published manuscripts devoted to each for further details. A detailed description of the framework implementation is given in Section 2.1. The process is captured by models for powder spreading (Section 2.2.1), heat source and paired thermal-fluid modeling (Section 2.2.2), and grain growth during solidification (Section 2.2.3). The mechanical response prediction consists of reduced order modeling (Section 2.3.2), constitutive law (Section 2.3.1), and performance metric (Section 2.3.3). The example results are shown in Section 3, with output and discussion for each model. The specific models that we use are selected to capture microstructure-level variations caused by the AM process and the impact of these variations on mechanical properties. These choices are not unique but simply elucidate the framework: this framework could also, for example, be used with part-scale thermodynamic simulations coupled to conventional continuum plasticity modeling, with local material properties dependent upon the information derived from processing, e.g. phase fraction [21]

2.1. Framework implementation

The general framework depicted in Fig. 2 contains mechanisms for input and output handling as well as intermediate storage. The solution domain is represented within a fixed format, flat file database as a regular grid of volume filling points, with each point described by coordinates (x, y, z location) to identify the unique record, each of which has fields that contain a datum: temperature at a point in time, phase, orientation, various stress and strain

x	y	z	T(t=0)	T(t=dt)	...	T(t=tend)	phase	orientation1	...	stress1	...
1	1	1	—	—	—	—	—	—	...	—	...
1	1	2	—	—	—	—	—	—	...	—	...
⋮	⋮	⋮	⋮	⋮	⋮	⋮	⋮	⋮	⋮	⋮	...
l	m	n	—	—	—	—	—	—	...	—	...

Fig. 3. A schematic of the flat file database used to store record data for the proposed framework. The fields are abbreviated to more clearly show the structure of the database.

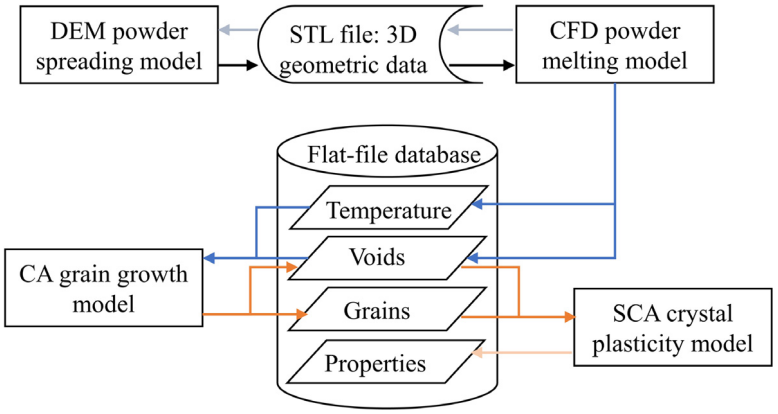

Fig. 4. Schematic diagram of data flow within the one-way coupled framework. Arrows with the same color show the data flow between models. (For interpretation of the references to color in this figure legend, the reader is referred to the web version of this article.)

tensors expressed componentwise, and a fatigue indicating parameter (FIP) in this implementation. These field values are chosen to match the information required by all of the models used, and are not necessarily unique or optimal in their ability to describe the process. Fig. 3 outlines the database format.

In this paper, the integrated framework is mainly based on one-way coupling as illustrated in Fig. 4, which is relatively straightforward to implement and test. Each model is directly connected to the next by passing output information to a subsequent input processor: the CFD powder melting model feeds temperature profiles and voids information to the CA grain growth model through the flat file database, and the CA grain growth model feeds the grains and void information to the SCA crystal plasticity model, also through the flat file database. In this case, data is promulgated in predominately one direction (process to structure to properties): a "backwards" coupling (e.g. structure to process) is not considered. Latent heat is considered an effective simplification of the influence of microstructure evolution on the temperature field and molten pool flow. Previous thermal or thermal-fluid models with this simplification have shown simulated temperature history and molten pool behavior in good agreement with experiments [22,5,7]. Published grain growth models [23,24] have also shown qualitative agreement with experimental results using simple one-way coupling that does not incorporate the influence of mechanical deformation (e.g., thermal stress) on grain growth. Therefore, this sequentially coupled framework should be sufficient to predict the temperature profiles, material structures and mechanical behaviors. From a top-down approach as illustrated below, this framework can be used to derive process–structure–property relationships, while a bottom-up approach could be used to solve design and inverse problems. Specifically, the framework proceeds as follows:

- The powder spreading model and powder melting model exchange high-resolution geometry information of the powder bed, using an STL-format surface mesh representation. That is, the DEM powder spreading model generates the particle packing configuration within one powder layer, outputs as an STL file, and feeds into the CFD powder melting, thereby reproducing powder spreading and melting, as illustrated by the black arrows in Fig. 4; the CFD powder melting model predicts the solidified shape, outputs as an STL file, and feeds into the DEM powder spreading model to apply a new powder layer, thereby reproducing powder spreading, as illustrated by the gray arrows in Fig. 4. The manufacturing process of multiple layers and tracks can be represented by repeating these two simulations and the data exchange between them.

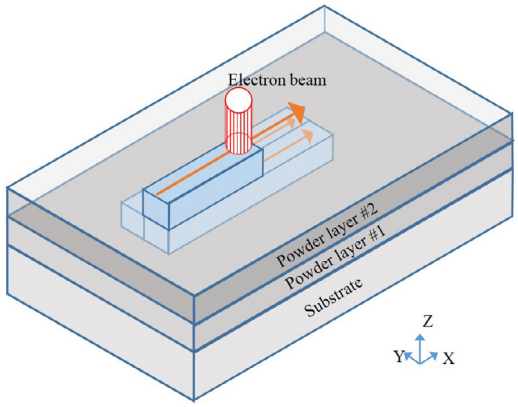

Fig. 5. Schematic of the Z-pattern electron beam scan strategy.

- The temperature profile in the volume of interest (VOI) is predicted by the powder melting model and written to a database in the flat file format shown in Fig. 3. By convention, void space is set to an ambient temperature to distinguish it from the dense material.
- The grain growth model reads the temperature field history from the database, and interpolates to match the grid spacing if needed. The dense material and voids are identified based on the temperature. Voids and free surfaces are thereby included in the grain growth model.
- The grain growth model simulates the grain growth process, predicts grain structure (phase and orientation), and writes grain and void information into the database.
- A sub-domain of particular interest, e.g. the largest void, of the full VOI for the grain growth model is selected as the input to the mechanical model; the grain and void information provided at each point via the database are interpreted as the center point of each voxel in a regular, uniform, cuboid mesh. This mesh can be used for all three mechanical response modules: FEM, SCA, and fatigue prediction.
- The SCA and FEM models are used to predict stress–strain response, which is added to the database.
- The fatigue prediction model reads the stress–strain behavior at each point, and computes a non-local potency estimate. The fatigue life of the highest potency location is computed to provide a scalar material response metric.

2.2. *Process modeling hub*

The first hub codifies the process models. Inputs include process conditions and material information. Process conditions incorporate a multitude of factors, such as the scan pattern, input power, powder bed thickness, and build chamber conditions (e.g. temperature, degree of vacuum).

In the relatively simple case shown here, the scan pattern is a two-pass, two-layer Z configuration: each layer is added using the same path at the new height. A diagram of the scan pattern is shown in Fig. 5. Between layers the powder spreading model is used to place the new bed of powder particles. The temperature history of each point and the final geometry of the CFD powder melting simulation are output information, which are subsequently used as the input to the grain growth model. The grain growth model input processor identifies the voids and predicts the grain structures based on thermal information from the CFD model. The output of this hub is the overall microstructure information, crystallography and geometry, predicted with the thermal–CFD model and grain growth model.

A continuum-based thermal model using the Finite Element Method (FEM), for example, could replace the thermal predictions of the high-fidelity thermal–CFD model used here. In this study, the high-fidelity models for powder spreading and melting are intended to provide a relatively accurate description of the thermal conditions and void information compared to the simpler models required for part-scale analysis. These high-fidelity models have high computational cost, limiting the total volume of material that can be investigated in the following examples.

Table 1
Material parameters of Ti–6Al–4V for the powder spreading model.

Property	Value
Density (ρ)	4000 kg/m^3
Young's modulus (E)	124 GPa
Poisson's ratio (υ)	0.41
Sliding friction coefficient (μ_f)	0.5
Restitution coefficient (θ)	0.5
Surface energy density (Ψ)	0.0002 J/m^2

Table 2
Input and output for powder spreading model.

Input	Particle size distribution
	Spreading tool geometry/description
	Substrate shape/material
Output	Powder bed state (STL geometry) after spreading

2.2.1. Powder spreading

The arrangement of particles in the powder bed is determined with a DEM-based particle spreading simulation. The distribution and dynamics of particles within the bed or on a substrate can influence the final build condition, e.g. through surface roughness or defect formation between tracks or layers [25]. Thus, spreading is simulated with accurate process variables such as the rake geometry, substrate geometry, layer thickness, powder size distribution, and frictional contact/collisions between particles and with the rake. The Hertz–Mindlin contact model ($\boldsymbol{F_n}$ and $\boldsymbol{F_t}$ are the normal and tangential contact forces) is defined by the equations in Eq. (1). This consists of nonlinear deformation and damping, where δ_n and $|\xi_t|$ are relative displacements, $|\dot{\delta_n}|$ and $|\dot{\xi_t}|$ are velocities, K_n and K_t are effective stiffnesses, and γ_n and γ_t are damping coefficients in the normal ($\boldsymbol{e_n}$) and tangential ($\boldsymbol{e_t}$) directions. Frictional sliding is (μ_f), and cohesive force is ($\boldsymbol{F_{JKR}}$) between fine particles, where m_1, m_2, and R_1, R_2 are the masses and radii of two contacting particles, and the contact area has a radius of a. The material parameters used in the model are listed in Table 1. Further details can be found in [26]. In this case, particles are spherical, and have diameters following a Gaussian distribution between 30 and 50 μm. A collection of particles is generated, dropped on the previous layer, and spread with a rake (see Table 2). A surface mesh, stored in an STL-format file, represents the resulting geometry.

$$
\begin{cases}
\boldsymbol{F_n} = (-K_n\delta_n^{3/2} - \gamma_n|\dot{\delta_n}|)\boldsymbol{e_n}, \\
\boldsymbol{F_t} = -(K_t|\xi_t| + \gamma_t|\dot{\xi_t}|)\boldsymbol{e_t}, \boldsymbol{F_t} \le -\mu_f|F_n|\boldsymbol{e_t}, \\
K_n = \dfrac{2E}{3(1-\upsilon^2)}\sqrt{\dfrac{R_1R_2}{R_1+R_2}}, \\
K_t = \dfrac{2E}{(2+\upsilon)(1-\upsilon)}\sqrt{\dfrac{R_1R_2}{R_1+R_2}\delta_n}, \\
\gamma_n = -\sqrt{\dfrac{5}{6}}\dfrac{\ln(\theta)}{\sqrt{\ln^2(\theta)+\pi^2}}\sqrt{3K_n\dfrac{m_1m_2}{m_1+m_2}}, \\
\gamma_t = -\sqrt{\dfrac{5}{6}}\dfrac{\ln(\theta)}{\sqrt{\ln^2(\theta)+\pi^2}}\sqrt{2K_t\dfrac{m_1m_2}{m_1+m_2}}, \\
\boldsymbol{F_{JKR}} = 4\sqrt{\dfrac{\pi a^3\Psi E}{2(1-\upsilon^2)}}\boldsymbol{e_t}.
\end{cases}
\tag{1}
$$

2.2.2. Powder melting

The STL file representing powder configuration is passed to a coupled thermal-fluid solver to compute thermal response and material redistribution during melting and subsequent re-solidification. The governing equations are

Table 3
Build parameters for cases 1 and 2.

Parameter	Case 1	Case 2
Hatch spacing	200 μm	240 μm
Electron beam power	60 W	60 W
Hatch strategy	Z-pattern	Z-pattern
Scan speed	0.5 m/s	0.5 m/s

continuity, momentum conservation and energy conservation, given by

$$\begin{cases} \nabla \cdot (\rho \boldsymbol{v}) = 0, \\ \dfrac{\partial}{\partial t}(\rho \boldsymbol{v}) + \nabla \cdot (\rho \boldsymbol{v} \otimes \boldsymbol{v}) = \triangledown \cdot (\mu \nabla \boldsymbol{v}) - \nabla p + \rho \boldsymbol{g} + \boldsymbol{f_B}, \\ \dfrac{\partial}{\partial t}(\rho h) + \nabla \cdot (\rho \boldsymbol{v} h) = q + \nabla \cdot (k \nabla T), \end{cases} \tag{2}$$

where flow is assumed to be incompressible, laminar, and Newtonian; in the momentum conservation equation, the major driving forces are incorporated, including gravity ($\boldsymbol{g}$), buoyancy ($\boldsymbol{f_B}$, Boussinesq approximation), viscosity (μ), recoil pressure, surface tension and Marangoni forces. The solid phase is approximated as a fluid with extremely large viscosity. Input energy (q) from an electron beam, heat conduction (where k is the thermal conductivity), and latent heat of phase change (captured in the definition of enthalpy h) are incorporated in the energy conservation equation. Surface convection is obviated due to the evacuated environment. An important term is that of the heat source (q), representing an electron beam impinging upon the bed of particles. A volumetric heat source model has been derived based on nano-scale simulations of electron–atom interactions in our previous study [27,28], and is given by:

$$q = \eta Q F_{section} F_{pene} \tag{3}$$

where q is the absorbed energy density, $F_{section}$ is the absorbed energy distribution within the beam cross-section, F_{pene} is the absorbed energy distribution along the penetration depth, η is the energy absorptivity, and the beam power Q is the product of the acceleration voltage and beam current. Further details can be found in [27,28]. The results shown in the following sections are for Case 1 in Table 3. The absorptivity, η, depends strongly upon the local incident angle and thus varies widely [27,28].

The fully coupled thermo-fluid flow equations governing the evolution of powder particles are computed with a finite volume method (FVM). Within this, the free surface is tracked using the volume of fluid (VOF) method,

$$\frac{\partial F}{\partial t} + \nabla \cdot (F \boldsymbol{v}) = 0 \tag{4}$$

where F represents the fluid volume fraction. At each time step, the free surface is reconstructed with VOF, the heat source in each computational cell is applied using the heat source model described above, the effects of evaporative mass loss, energy loss and recoil pressure on the free surface are computed on each cell, and the free surface is updated. Further details can be found in [6,26]. For these simulations, the material parameters are given in Table 4. A list of the inputs and outputs of this module is provided in Table 5. The cell size for this model is 5 μm: sufficient to eliminate mesh sensitivity, based on a previous study [28]. The computation time for the 2-layer, 2-track case (see Fig. 5) is around 700 h on a desktop computer using an Intel Core i7-2600 CPU.

The temperature history of each computational cell is output into the flat file database for use in the CA model. To distinguish between a solid/liquid domain and void space, i.e. above the build surface and any voids within the material, void areas are assigned ambient temperature, while the temperature of the solid/liquid domain is no lower than the initial temperature (about 900 K) due to the preheating procedure in SEBM.

2.2.3. Grain growth

Grain formation during solidification can be computed based on the temperature field input in the flat file format, which is originally provided by the thermal–CFD module. While various models (e.g., Kinetic Monte Carlo model [23]) can be potentially implemented into this framework, a cellular automaton (CA) model is used in this work [29]. In the CA model, the material region is discretized by a set of cubic cells of 1.25 μm. A decentered

Table 4
Thermal and flow properties of Ti–6Al–4V [4].

Property	Value
Density (ρ)	4000 kg/m^3
Solidus temperature (T_s)	1878 K
Liquidus temperature (T_l)	1928 K
Latent heat of melting (L_m)	2.86×10^5 J/kg
Latent heat of evaporation (L_v)	9.7×10^6 J/kg
Saturated vapor pressure (P_{s0}) at $T_0 = 3315$ K	1.013×10^5 Pa
Specific heat (c)	872 J/(K kg)
Thermal conductivity at solidus (k)	16 W/(m K)
Thermal conductivity at liquidus (k)	32 W/(m K)
Surface radiation coefficient (α_b)	0.4
Surface tension coefficient (σ)	1.68 N/m
Temperature sensitivity of σ (σ_s^T)	0.00026
Viscosity (μ)	0.005 Pa s
Domain size	2.5 mm × 1 mm × 0.45 mm
Mesh	500 × 200 × 90
Cell size	0.005 mm

Table 5
Input and output for thermal–CFD model.

Input	Powder bed state
	Thermal processing conditions
	Material properties
Output	Thermal history of each point in the volume
	Geometry (including voids)

Table 6
Input and output for grain growth model.

Input	Thermal history at each point
	Material properties, parameters
Output	Phase ID (includes void phase)
	Grain orientation (Bunge Euler angles)

octahedron growth method, proposed by Rappaz and Gandin [29], is used to compute the new envelope during grain growth. This approach was shown by those authors to avoid the anisotropy that might otherwise be inherent in the cell lattice structure. The mesh size was selected based on our previous study [30] to avoid mesh sensitivity. The temperature history of each cell is determined from the thermal–CFD simulation using a linear interpolation. More details can be found in forthcoming work [31]. The input and output of this module are summarized in Table 6.

There are two main sub-models required for the CA model. The first, a heterogeneous nucleation model, consists of defining the distribution of nucleation sites, the critical undercooling value (the temperature at which nucleation occurs at each site), and the crystal orientation of newly nucleated grains. In this CA model, nucleation occurring at the boundary of a liquid volume is treated differently from nucleation within the bulk of the liquid volume through a "wall" nucleation density $n_{max,w}$ with units of m^{-2} and a "liquid", or bulk, nucleation density $n_{max,l}$ with units of m^{-3}. Prior to the simulation, the total number of nucleation sites at the surface and in the bulk are calculated and assigned critical undercooling values. This critical undercooling varies from site to site; the variation is assumed to follow a Gaussian distribution (given by the values of the mean, $\overline{\Delta T}$, and standard derivation, ΔT_σ). The surface and bulk nucleation sites may use different values of $\overline{\Delta T}$ and ΔT_σ, distinguished by subscripts w and l.

The second sub-model, a model of grain growth during the solidification process, controls the rate and direction for which existing grains grow by assimilating surrounding cells. For a newly nucleated grain, the initial dendritic network within the cell is assumed to be a regular octahedral envelope bounded by ⟨111⟩ planes and to have a random crystallographic orientation defined by a set of Euler angles. The six half-diagonals of the octahedron correspond to the primary dendritic growth directions of the grain. Grain growth is simulated by extending these half-diagonals

Table 7
CA model parameters; material parameters from [33].

Parameter (s)	Value (s)
T_{melting}	1928 °C
T_{ambient}	298 °C
Domain size	0.35 mm × 0.225 mm × 0.055 mm
Mesh size	280 × 180 × 44
Cell edge size	1.25×10^{-3} mm
Nucleation, wall: $n_{max,w}$, $\overline{\Delta T}_w$, $\Delta T_{w,\sigma}$	5×10^{10} m^{-2}, 2 °C, 0.5 °C
Nucleation, liquid: $n_{max,l}$, $\overline{\Delta T}_l$, $\Delta T_{l,\sigma}$	5×10^{14} m^{-3}, 2 °C, 0.5 °C
Growth rate: a_3, a_2, a_1	0.0, 2.03×10^{-4} m/(s °C^2), 0.544×10^{-4} m/(s °C)

based on the dendrite tip velocity, $v\,(\Delta T)$. Here ΔT is the local undercooling at the center of the cell that owns the envelope; ownership is determined by a decentered octahedron growth algorithm [29]. As time proceeds, the envelope grows and eventually engulfs neighboring cells to propagate the grain. For an active envelope located in a cell, e.g. cell i, the change in length of its diagonal, ΔL_i, is calculated as

$$\Delta L_i = v\,(\Delta T_i)\,\delta t \tag{5}$$

where ΔT_i is the total undercooling at the center of the cell and δt is the current time step. The growth rate, $v\,(\Delta T_i)$, is usually estimated based on the undercooling by a polynomial formulation. We use

$$v\,(\Delta T) = a_1 \Delta T + a_2 \Delta T^2 + a_3 \Delta T^3, \tag{6}$$

where a_1, a_2 and a_3 are fit parameters calibrated to experimental or theoretical results based on the dendrite tip growth kinetics [32,33]. The parameters for this portion of hub 1 are provided in Table 7. Dezfoli et al. derive the CA model parameters specific to Ti–6Al–4V used here [33], where $a_3 = 0.0$.

The conditions of AM (high temperature gradient and cooling rate) result in grain growth dominated by epitaxial growth from existing grains surrounding the melt pool. Thus, the grain structure of the substrate and metal powders are obtained first through the nucleation parameters shown in Table 7 before the melting process; during the melting and re-solidification process, nucleation is assumed to progress only from the solid material boundary to better capture growth conditions under AM. For more details see [30]. The prediction results from the CA model are written to the database as a phase ID (a unique integer) and a predicted crystallographic orientation (Euler angle triplet following the Bunge convention) for each voxel in the CA domain. This database can be read directly to construct a voxel mesh, since material properties are associated with phase ID and orientation.

2.3. Mechanical response prediction hub

The second hub codifies our mechanical response and performance prediction methods. Input to this hub is crystallographic and geometric microstructure information, as well as material properties for constitutive model calibration. The output of this hub is a prediction of mechanical response, i.e. overall stress–strain curves, local plastic strains and stresses, and the high-cycle fatigue incubation life. All information (phase ID, grain orientation, etc.) is carried by voxels. A state-of-the-art reduced order modeling scheme called Self-consistent Clustering Analysis (SCA) [34,35] was used to speed up our simulations. Volumes of interest (VOIs) for computing the fatigue indicating parameter (FIP) and predicting fatigue life are selected from the larger thermal–CFD-grain growth region; a subset with known spatial coordinates can simply be queried from the database, which contains the predicted microstructure (void size, shape, location, grain size, shape, orientation, etc.). All the input and output data to and from this module is listed in Table 8.

2.3.1. Crystal plasticity for material law

To understand the microscale mechanics, in this case the influence of unusual grain geometry and the relatively frequent occurrence of voids in AM, we apply a crystal plasticity (CP) constitutive law. In the CP framework, deformation is described by summing the shear slip rate of all slip systems in all the crystals under

Table 8
Input and output for mechanical response model.

Input	Phase ID (including voids)
	Grain orientations (if not provided assume single crystal in weakest orientation)
	Material properties
	Boundary/loading conditions (assumes periodic BCs)
Output	Stresses
	Strains

consideration:

$$\tilde{\boldsymbol{L}}^{p} = \sum_{\alpha=0}^{N_{slip}} \dot{\gamma}^{(\alpha)} \left(\tilde{\boldsymbol{s}}^{(\alpha)} \otimes \tilde{\boldsymbol{m}}^{(\alpha)} \right) \tag{7}$$

where $\tilde{\boldsymbol{L}}^{p}$ is the plastic velocity gradient in the intermediate configuration (as described in [36]); α is the index of a slip system; $\dot{\gamma}^{(\alpha)}$ is the rate of shear slip in slip system α; $\tilde{\boldsymbol{s}}^{(\alpha)}$ is the slip direction of that system and $\tilde{\boldsymbol{m}}^{(\alpha)}$ is the slip plane normal. In the model used here, a simple rate-dependent power-law with backstress governs the rate of shear slip:

$$\dot{\boldsymbol{\gamma}}^{(\alpha)} = \dot{\gamma}_0 \left| \frac{\tau^{(\alpha)} - a^{(\alpha)}}{\tau_0^{(\alpha)}} \right|^{(m-1)} \left(\frac{\tau^{(\alpha)} - a^{(\alpha)}}{\tau_0^{(\alpha)}} \right) \tag{8}$$

where $\dot{\gamma}_0$ is a reference shear strain rate, $\tau^{(\alpha)}$ is the resolved shear stress on slip system α, $a^{(\alpha)}$ is a backstress for kinematic hardening, and $\tau_0^{(\alpha)}$ is the reference shear strength, the evolution of which depends on the terms for direct hardening and dynamic recovery in a hardening law [37]. The reference shear strength $\tau_0^{(\alpha)}$ evolves based on the expression

$$\dot{\tau}_0^{(\alpha)} = H \sum_{\beta=1}^{N_{\text{slip}}} q^{\alpha\beta} \dot{\gamma}^{(\beta)} - R \tau_0^{(\alpha)} \sum_{\beta=1}^{N_{\text{slip}}} |\dot{\gamma}^{(\beta)}|, \tag{9}$$

where H is the direct hardening coefficient and R is the dynamic recovery coefficient and $q^{\alpha\beta}$ is the latent hardening ratio given by:

$$q^{\alpha\beta} = \chi + (1 - \chi)\delta_{\alpha\beta} \tag{10}$$

where χ is a latent hardening parameter (1: without latent hardening, 0: with latent hardening). The backstress $a^{(\alpha)}$ evolves based on the expression:

$$\dot{a}^{(\alpha)} = h \dot{\gamma}^{(\alpha)} - r a |\dot{\gamma}^{(\alpha)}|, \tag{11}$$

where h and r are the direct hardening and dynamic recovery factors respectively.

It has been observed that the microstructure of Ti–6Al–4V produced by SEBM is dominated by hexagonal-close-packed (hcp) α grains which are transformed from the prior body-centered-cubic (bcc) β grains. The α phases originating from the same parent β grain have similar orientation [38]. For this demonstration of the framework we make the simple, though inaccurate, assumption that each parent β grain, under thermal processing, produces a single, aligned child α grain. Slip systems used for the dominant α-phase of Ti–6Al–4V are $3\langle 11\bar{2}0\rangle\{0001\}$ basal, $3\langle 11\bar{2}0\rangle\{10\bar{1}0\}$ prismatic, $6\langle 11\bar{2}0\rangle\{10\bar{1}1\}$ first order pyramidal and $12\langle 11\bar{2}3\rangle\{10\bar{1}1\}$ second order pyramidal. These are shown in Table 9, as provided by [39]. Parameters for the crystal plasticity material model used both for offline and online stages are also given in Table 9, where C_{ij} are the stiffness components in Voigt notation [36].

2.3.2. Self-consistent clustering analysis

The boundary value problem of the VOI to be solved can be written in a Lagrangian formulation as:

$$\begin{cases} \mathbf{div}\, \boldsymbol{\sigma}(\boldsymbol{x}) = 0, \forall \boldsymbol{x} \in \Omega \\ \boldsymbol{\sigma}(\boldsymbol{x}) = \mathbf{f}(\mathbf{x}, \boldsymbol{\epsilon}, \dot{\boldsymbol{\epsilon}}, \mathbf{s}) \\ \boldsymbol{\epsilon} = \boldsymbol{\epsilon}^{*} + \bar{\boldsymbol{\epsilon}} \end{cases} \tag{12}$$

Table 9
Calibrated elastic and plastic crystal plasticity parameters for primary α phase.

Elasticity:	MPa	Plasticity:				
C[a]		Phase	Basal	Prismatic	Pyramidal $\langle a \rangle$	Pyramidal $\langle c+a \rangle$
$C_{11} = C_{22}$	1.7×10^5	$\dot{\gamma}_0$[a] s^{-1}	0.0023	0.0023	0.0023	0.0023
C_{33}	2.04×10^5	m[a]	50	50	50	50
$C_{44} = C_{55}$	1.02×10^5	τ_0 MPa	284.00	282.24	395.00	623.30
C_{66}	0.36×10^5	$a^{t=0}$ MPa	0.0	0.0	0.0	0.0
$C_{12} = C_{21}$	0.98×10^5	H MPa	1.0	1.0	1.0	1.0
$C_{13} = C_{31}$	0.86×10^5	R MPa	0.0	0.0	0.0	0.0
$C_{23} = C_{32}$	0.86×10^5	h MPa	500.0	500.0	500.0	500.0
Other C_{ij}	0	r MPa	0.0	0.0	0.0	0.0
		χ	1.0	1.0	1.0	1.0

[a] Parameters are from [39]. Others are selected to match experimental results.

Table 10
Offline and online model parameters.

Parameter (s)	Value (s)
Domain size	0.05 mm × 0.05 mm × 0.05 mm
Mesh size	40 × 40 × 40
Element edge length	1.25×10^{-3} mm
Material law, offline	linear elasticity
Material law, online	crystal plasticity
Strain amplitude, online	0.5%, 0.375%, 0.3%
№ of strain cycles	4
Load ratio, $R = \epsilon_{min}/\epsilon_{max}$	-1
Strain rate, $\dot{\epsilon}$	0.1 s^{-1}

where $\boldsymbol{x}$ is a point in the VOI Ω_0; $\boldsymbol{\sigma}(\boldsymbol{x})$ is the local stress tensor, which is a function of the local strain $\boldsymbol{\epsilon}$, its rate $\dot{\boldsymbol{\epsilon}}$ and some internal variables $\mathbf{s}$ for a general elasto-viscoplastic material. The local strain $\boldsymbol{\epsilon}$ is the sum of a fluctuating term $\boldsymbol{\epsilon}^*$ and a prescribed overall strain $\bar{\boldsymbol{\epsilon}}$. Assuming periodic boundary conditions, the above boundary value problem is equivalent to the following Lippmann–Schwinger formulation [40]

$$\boldsymbol{\epsilon} = -\boldsymbol{\Gamma}^0 * (\boldsymbol{\sigma} - \mathbf{C}^0 : \boldsymbol{\epsilon}) + \bar{\boldsymbol{\epsilon}}, \tag{13}$$

where $\boldsymbol{\Gamma}^0$ is the Green's operator corresponding to the reference stiffness $\mathbf{C}^0$ and $*$ denotes the convolution operation.

The reduced order mechanical modeling scheme used here is based on discretization of the Lippmann–Schwinger formulation. The way this approach differs from other reduced order methods is that the decomposition of the VOI is based on knowledge of the strain concentration. This is used to group regions of material with similar deformation behavior. This information is acquired in the "offline" stage of the SCA approach, where a simple (elastic) direct numerical simulation of the microstructure of interest is conducted. In the "online" stage, any nonlinear material law and/or loading path can be used. The implementation of CP within SCA is given in [41].

In this case, the strain concentration tensor of each voxel is obtained with a linear elastic finite element model conducted in Abaqus using C3D8R elements. This model computes the elastic response of a VOI with periodic boundary conditions under three uniaxial tensile loading cases (corresponding to x, y, z directions respectively). The stretch direction is the same as applied during the online stage. The elastic strains thus obtained are used in a k-means clustering algorithm for domain decomposition, where the squared Euclidean distance measure is used for clustering.

Four fully-reversed unidirectional load cycles at various strain amplitudes with crystal plasticity constitutive law were simulated during the online analysis. These cycles result in a stabilized value of $\Delta\gamma^p_{max}$ and a known σ^n_{max}, used later to compute a FIP. A full accounting of the parameters used for both the offline and online modules is provided in Table 10.

2.3.3. Performance prediction: fatigue life

A performance metric simplifies ranking the predicted build quality of a part or process parameter set to the comparison of a scalar factor. To provide a metric, this module estimates the high-cycle fatigue life of the predicted

Table 11
Input and output for fatigue prediction.

Input	Stresses
	Strains
	Material properties
Output	FIP
	N_{inc}

microstructure. A Fatemi–Socie FIP appropriate for microstructural analysis is used, which is given by

$$FIP = \frac{\Delta\gamma^p_{max}}{2}\left(1 + \kappa\frac{\sigma_n^{max}}{\sigma_y}\right) \tag{14}$$

where $\Delta\gamma^p_{max}$ is the maximum of the cycle-to-cycle change of the plastic shear strain, σ_n^{max} is the stress normal to $\Delta\gamma^p_{max}$, σ_y is the yield stress, and κ is a normal stress factor, taken to be 0.55 [42,43]. The value of $\Delta\gamma^p_{max}$ saturates after a few load cycles and the saturated value can be used to compute FIP and N_{inc} [37]. The relationship between FIP and N_{inc} for Ti–6Al–4V is calibrated to experimental high cycle fatigue life data for wrought (nominally defect free) Ti–6Al–4V presented by [44]. Here, this calibration has been done to reduce the total RMS difference between the experimental data of [44] and the N_{inc} predicted for the polycrystalline, defect free VOI at 0.5% and 0.375% strain amplitudes simultaneously (this is the simulation condition that best matches that of the experimental conditions). A moving volume average with window size of about 10% of the volume of the microstructure of interest (e.g. the mean void size) is used to compute the nonlocal FIP. The maximum nonlocal FIP, $NFIP_{max}$, is correlated with fatigue crack incubation life, N_{inc}, through

$$NFIP_{max} = \bar{\gamma}_f(2N_{inc})^c \tag{15}$$

where $\bar{\gamma}_f$ and c, multiplicative and exponential factors, are used to fit experimental high cycle fatigue data. The fitted value of these factors is 0.006736 and -0.0238 respectively. The input and output of the module are summarized in Table 11.

3. Example results and discussion

The final result of this integrated framework is the computed performance metric. Here we also present intermediate results from each of the models described above, to make the flow of information between modules and hubs within the framework more clear by example. Each of the modules contains a state-of-the-art method in itself; the important point that we demonstrate, to our knowledge for the first time in the open literature, is that the modules used to predict processing and material response to mechanical loading during service have been directly linked. A comparison of the final metric for build quality between cases with different processing conditions is made. The examples here show the influence of process parameter choices on simulated performance with two distinct cases shown in Table 3: one with hatch spacing 200 μm and the other with hatch spacing 240 μm. This allows us to directly show the differences in that result from different process parameters. The influence can be seen in Fig. 14, where a larger hatch spacing results in the prediction of voids, reducing estimated fatigue life.

3.1. Powder spreading

The powder spreading model produces a relatively densely packed bed of particles, with random spatial distribution. Fig. 6(a) shows the powder arrangement for the first layer, spread on a smooth Ti–6Al–4V substrate. Fig. 6(b) shows the arrangement of particles for the second layer, spread upon the surface resulting from the thermal–CFD process simulation of the first layer. The surfaces shown in these figures are represented by STL meshes, and given thereby to the first step of the thermal–CFD code: a 3D mesh generator.

3.2. Powder melting

The geometry generated by the powder spreading model has been fed into the powder melting model, and the solidified shape has been simulated as shown in Fig. 8 for Case 2 in Table 3. Note the match between the unmelted

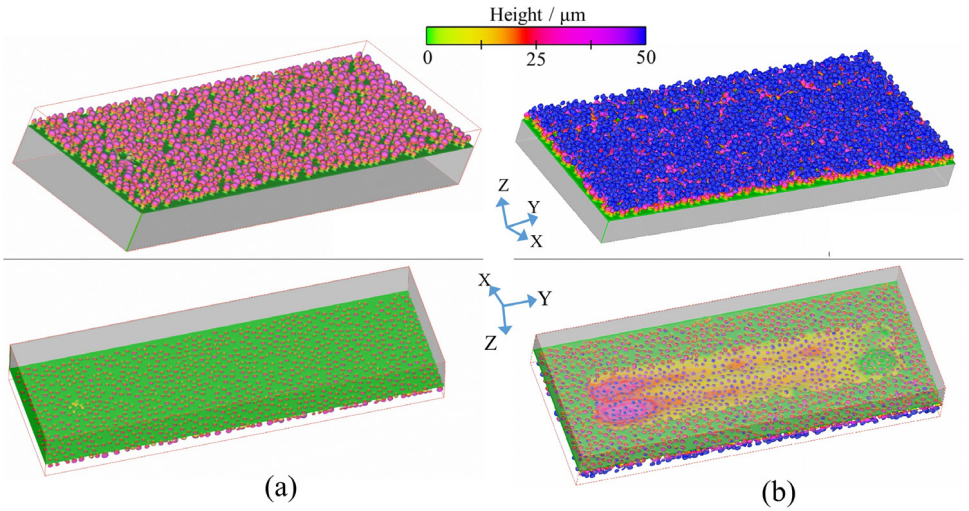

Fig. 6. Powder bed configurations generated by powder spreading simulations. (a) The first powder layer with a thickness of 0.05 mm spread on the substrate. (b) The second powder layer with a thickness of 0.05 mm spread on the solidified surface of the first layer. The figures are colored by the height from the substrate surface. In (a) and (b), the upper sub-figures show views from above, and the lower ones show views from below (the z-direction), with the non-powder material hidden. (For interpretation of the references to color in this figure legend, the reader is referred to the web version of this article.)

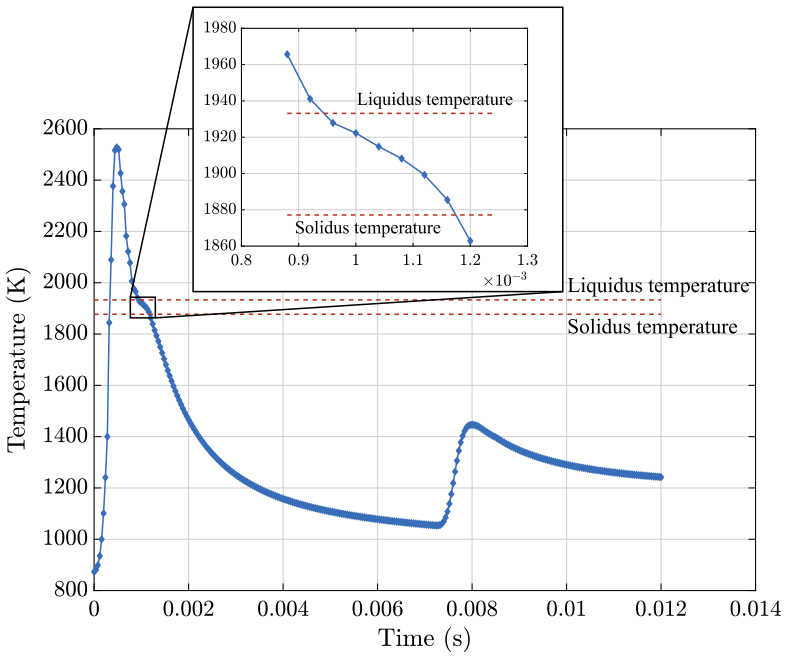

Fig. 7. Example temperature history taken from a single point of the thermal–CFD simulation. The inset curve highlights the kink caused by latent heat.

portions of Fig. 8 and the same locations in Fig. 6: the results from one model are used directly in the next. Fig. 7 shows an example of the temperature evolution at a single point. Rapid heating and cooling with a slight kink caused by the latent heat of solidification is predicted; the solidification kink is shown in detail in the inset. The temperature peaks again upon subsequent passes of the electron beam. This matches the well-documented thermal profile for SEBM, e.g. [2,45].

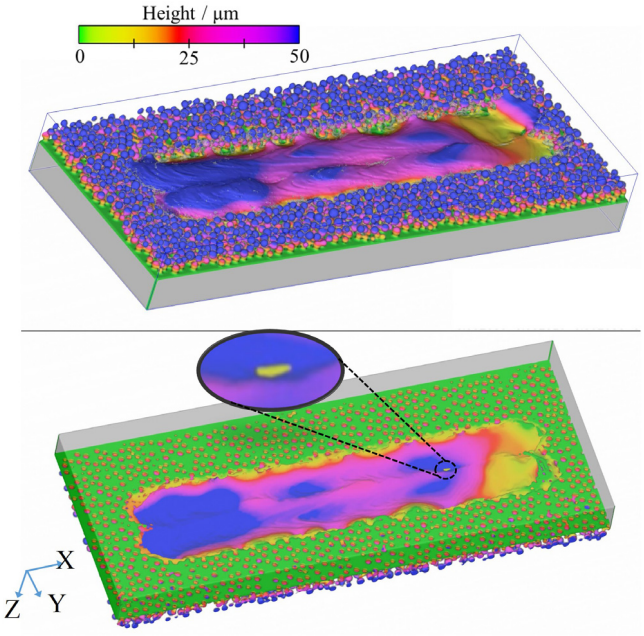

Fig. 8. Voids are observed in the CFD simulation of multiple-layer multiple-track manufacturing process. This is a 3D view of the free surfaces after manufacturing, colored by the height from the substrate surface. The upper image shows a view from above, and the lower image shows a view from below, with the substrate material hidden. The inset image highlights a void predicted during the build. (For interpretation of the references to color in this figure legend, the reader is referred to the web version of this article.)

A void predicted by the CFD model is highlighted in the inset in Fig. 8. These voids result from lack of fusion between particles near the boundaries between the melt tracks. The irregular shapes and positions (between tracks and layers) match qualitatively with lack of fusion voids observed experimentally, e.g. [46]. Because no vapor phase is explicitly included in this CFD model, no voids caused by entrained gas are predicted. Simulated builds with different conditions, e.g. Cases 1 and 2 in Table 3, result in different geometric configurations and thermal profiles, as shown in [28].

3.3. Grain growth

This model predicts solidification front motion and grain growth given the thermal history; Fig. 9(a) shows the molten pool temperature at $t = 0.157$ ms. Fig. 9(b–d) track the progression of the solidification front and the subsequent primary phase grain growth at $t = 0.234$ ms, $t = 0.438$ ms, and $t = 0.931$ ms. The simulation was run on six processors and took 13000 s. The initial grain structures of the substrate and powder particles were generated by a preliminary CA simulation using a uniform temperature and constant cooling rate of 20.3 K/ms with only bulk nucleation. The emergence of columnar grains from an existing substrate is captured with qualitative similarity to experimental results, e.g. [47] which reports the cubic β-grain structure that forms during initial solidification. The CA model captures the growth of the primary β-phase. Sub-granular structures, such as dendrites, are not considered explicitly and thus cannot be observed.

Grains appear tilted in the direction of the heat source motion, showing a trend also observed in experiments and other simulations of grain growth during AM (e.g. [47,33]). This is shown by the longitudinal cross section of the region of interest in Fig. 10. Fig. 11 shows a transverse cross section of the region with radial, epitaxial grain growth from the underlying material.

3.4. Mechanical response prediction

When run without the CA module, we assume a single crystal oriented such that the Schmid factors, the products of the slip plane and slip orientation cosines, are maximized: the weakest orientation, representing a “worst-case”

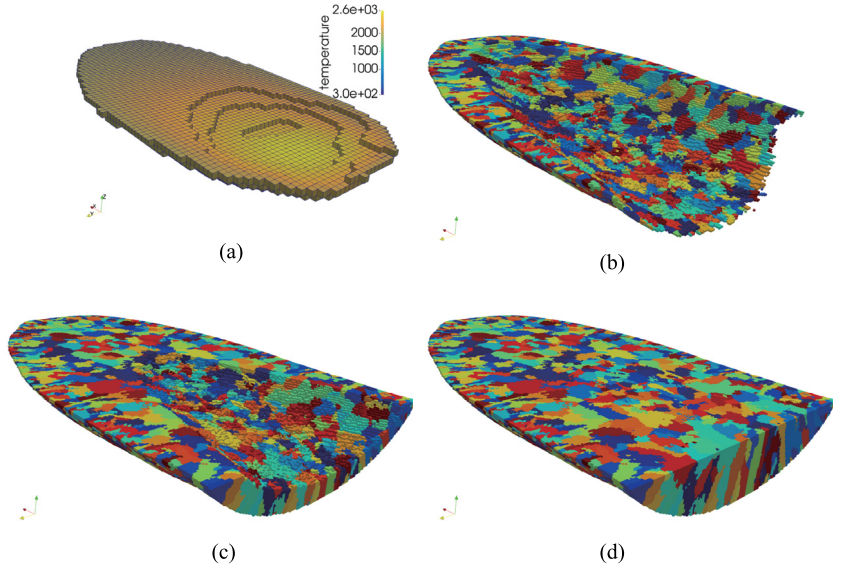

Fig. 9. (a) Molten pool profile colored by temperature at $t = 0.157$ ms and evolution of the subsequent solidification microstructure represented by three snapshots at relative time: (b) $t = 0.234$ ms, (c) $t = 0.438$ ms, and (d) $t = 0.931$ ms. Grain coloring is selected to maximize contrast between nearby grains. (For interpretation of the references to color in this figure legend, the reader is referred to the web version of this article.)

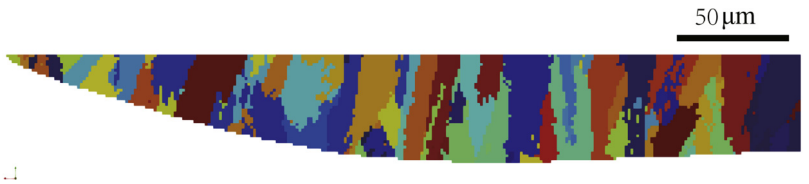

Fig. 10. Longitudinal cross section view of molten pool microstructure to show angled grain growth following the direction of motion of the heat source.

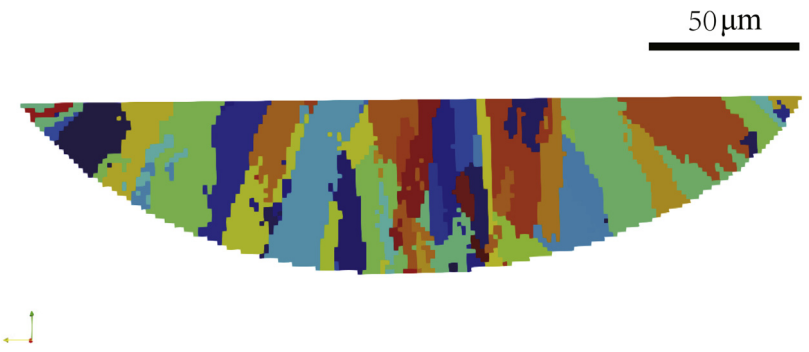

Fig. 11. Transverse cross section view of molten pool microstructure to show the radial distribution of grain growth.

analysis. A more realistic, polycrystalline grain structure enabled by the CA model allows us to capture some of the effects of the crystalline texture on the material response. Fig. 12(a) and (b) show four polycrystalline VOIs selected from the CA solution for a two-track, two-layer simulation. Three VOIs are selected throughout the height

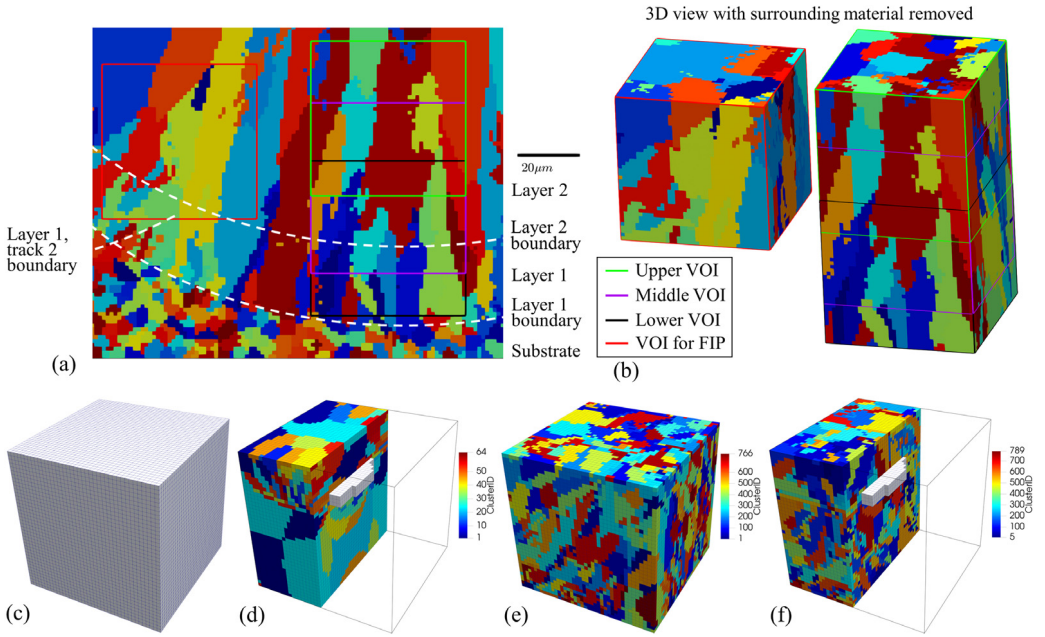

Fig. 12. (a) A 2D section of the CA result with the relative locations of four cubic VOIs at different locations through the height of a two-layer build (color coded green, purple, and black to upper, middle, and lower) and one near the intersection of two tracks of the same build (red; for FIP with/without void). The white dashed lines show approximate melt region boundaries for each layer. (b) These VOIs in 3D with the surrounding material removed. (c) The single crystal voxel mesh used for FIP prediction. (d) Clustering used for the single crystal, with a void (white) case. (e) The clusters used for the polycrystal case. (f) The clusters used for the polycrystal with void case. (For interpretation of the references to color in this figure legend, the reader is referred to the web version of this article.)

of the build (the black, purple, and green outlines) and a fourth VOI (red outline) is selected from the intertrack area. The fourth region in the CA volume is selected because the intertrack area contains a large void caused by lack-of-fusion, predicted by the thermal–CFD model, which influences the fatigue life of the component. The void space is represented by a unique phase ID in both the thermal–CFD results and the CA results and is interpreted as a void by the SCA model. When the framework is used without the CA model, the void space is directly passed to SCA, again through a unique phase ID in the voxel database, and is passed via the CA model when the CA model is used. Thus, the coupling of the framework is achieved by defining geometry and crystallographic information using the thermal–CFD and CA models and using the structures thus defined as the geometry and crystal orientation required by the crystal plasticity model. In the following examples, VOIs are selected to highlight spatial differences within the build, rather than to represent average material properties of an entire build. This is motivated by applications where failure is a concern, in which the local minimum properties are of greater importance than the mean properties.

3.4.1. Anisotropic response of the polycrystalline VOIs

For the polycrystalline case, where the CA model is employed, the anisotropic stress–strain response at the strain rate of 10^{-4} s^{-1} for the first three VOIs with loading in the x-, y-, and z-directions is shown in Fig. 13; an anisotropic and location dependent response emerges from the crystallographic structure. Each of these VOIs is 40 voxels $\times$ 40 voxels $\times$ 40 voxels. A voxelated mesh is constructed directly from the VOI, with material properties assigned to each voxel corresponding to the known properties for the crystal predicted by the CA model. The periodic boundary condition assumption can result in spurious stress localizations near the boundary of these volumes. To counteract this, the five surface layers of voxels are neglected for the results presented below. This is similar to the relatively common "buffer zone" approximation. The simulation was run on a single processor and each stress–strain curve took approximately 680 s in total with 600 s to calculate elastic strain concentration, 43 s to calculate interaction tensor and 27 s for online crystal plasticity analysis for 100 loading increments.

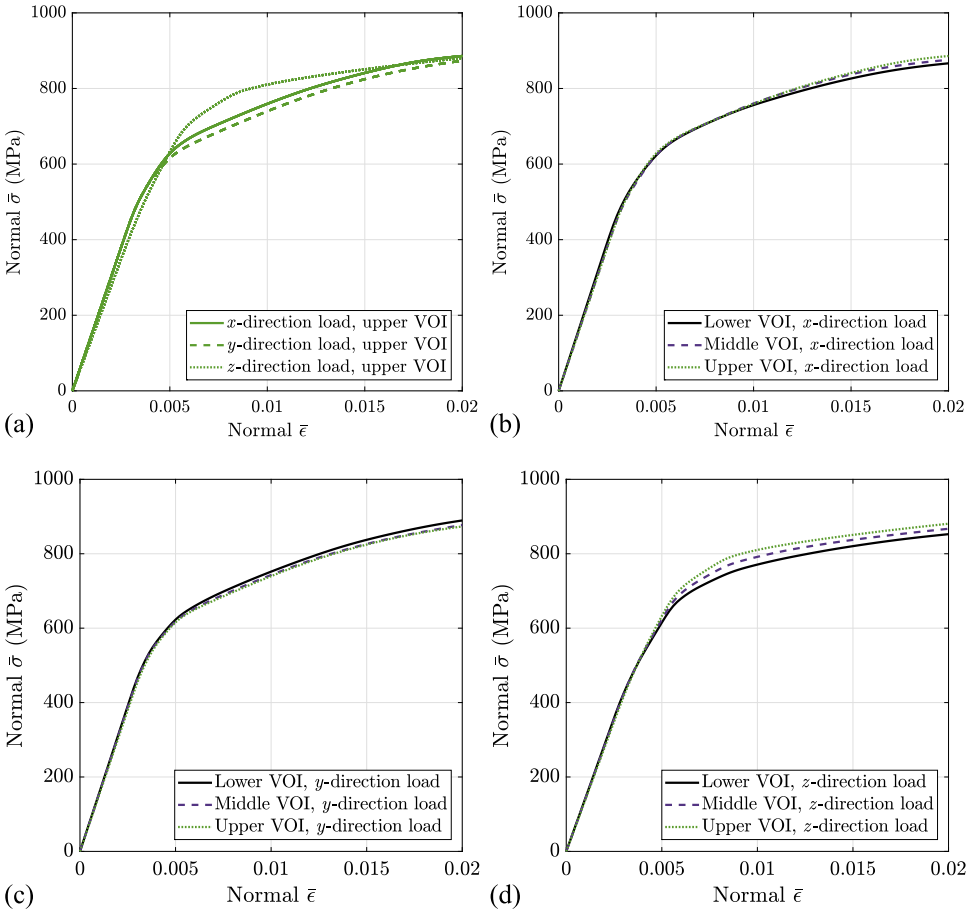

Fig. 13. Stress–strain curves predicted by SCA with CP at the strain rate of 10^{-4} s^{-1} (a) for the upper VOI showing the anisotropy of overall response, for all VOIs. The response for each VOI is given for x-direction loading (b), y-direction loading (c) and z-direction loading (d).

3.5. Performance prediction: fatigue crack incubation life

Relative values of N_{inc} or FIP can provide insight into the impact a particular defect, or perhaps a class of defects such as lack of fusion voids, has upon the expected lifetime of the material under cyclic loading. For example, here we compare the computed N_{inc} value for four different VOIs. The first two show results using the framework without the CA model, and the second two show results with the CA model. In each of these sets, one result is taken from Case 1 (which does not exhibit voids) in Table 3 and the other is from Case 2 (where voids are observed).

The first is a reference VOI: a simple single-crystal cube, representing a defect-free build (without the CA model). The second VOI is the same single-crystal cube, this time with a void predicted by the thermal–CFD model. This comes from Case 2 in Table 3, where larger hatch spacing results in insufficient fusion. The third VOI incorporates the CA model, making this a polycrystalline simulation. The fourth VOI adds the void to the polycrystalline volume. The simple, cubic voxel mesh underlying all four of these VOIs is shown in Fig. 12(c). The subsequent Fig. 12(d–f) show the clusters used for SCA, computed from the elastic DNS, for the latter three VOIs, respectively.

Fig. 14 shows the predicted strain-life behavior of these four VOIs. In the single crystal condition without a void there are no stress localizers, and the highest life is expected. The introduction of a void decreases the expected life substantially, as local stress concentrations occur around the void. In the polycrystalline VOI grain boundaries act as stress localizers, and even without a void the fatigue life is reduced from the reference VOI; however, the introduction of a void has less impact than in the single crystal VOI, since the worst case configuration – a high Schmid factor grain near the void – has not occurred. The extremely high predicted life at very low strain amplitude is likely because

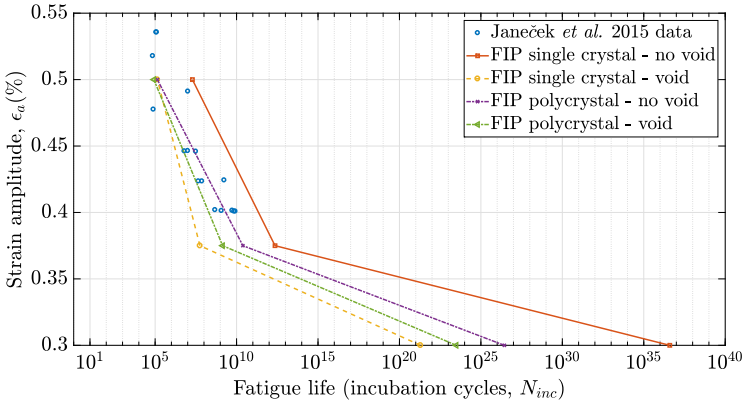

Fig. 14. Experimental strain life data (points) for HCF replotted from [44], and four predictions of fatigue life: (1) a single crystal without any defects (baseline data), (2) a single crystal with a void predicted with the thermal–CFD model and (3) the full polycrystalline fatigue VOI shown in Fig. 12 (4) this same growth pattern, including a void.

our current model does not capture the transition of failure mechanism thought to occur between high cycle fatigue and ultra-high cycle fatigue in Ti–6Al–4V [44]. While not necessarily meaningful, it does not impact the current demonstration of the framework unduly.

The trends between different cases match qualitatively with experimental results demonstrated for SEBM. For example, Li et al. [48] compare experimentally measured fatigue life of Ti–6Al–4V for numerous AM technologies, including SEBM in hot isostatic pressing (HIP), heat treated, and as-built conditions. Subjecting the material to HIP is known to suppress voids, whereas heat treatment and as-built material retains any voids introduced during manufacturing. Thus, HIP SEBM results and non-HIP SEBM results present in Li et al. are comparable to the polycrystal no-void and void results respectively shown in Fig. 14: in both the simulation and experiment reduction of void content results in higher fatigue life. A similar relationship, reduction of fatigue life with the introduction of a void, is presented by Gong et al. [49], where voids were intentionally built into a test coupon to study their effects.

This set of examples shows that the framework and models here can capture, at least qualitatively, the influence of process parameters (hatch spacing in the example shown) on expected material performance. This influence is captured by directly considering the change in material structure, i.e. the introduction of a void cause by lack of fusion, that results from a change in the processing conditions. The method presented is general: the impact of process parameter selection upon expected material performance can be predicted using this framework. Further, we have demonstrated that the framework is flexible enough that models can be added, removed, or exchanged depending on the level of detail desired. In this case, we show the framework operating both with and without a prediction of grain growth via the CA model.

3.6. Outlook

3.6.1. Outlook for the individual modules

The largest limitation of the thermal–CFD model currently is the lack of an explicit gas or vapor phase. This prohibits the prediction of pores due to entrained gas. Residual stress, an important factor in all AM processes, is also not captured. This important facet is the focus of ongoing work.

One limitation of the current grain formation model is the inability to predict solid-state phase transformations and grain coarsening during reheating. Thus, this prediction is thought to be applicable to the final layer of a build; reheating due to subsequent passes of the beam for interior layers is known to cause grain coarsening. However, the grain shape predicted is that of the β-phase (bcc), but α and $\alpha + \beta$ are known to be dominant in the final part. Under solid state phase transformations, the β to α transition creates smaller, α grains from the parent β-phase; from this, a material with mixed $\beta + \alpha$ is usually expected. There is ongoing work to develop a module that captures solid state phase transformations and grain coarsening effects, but this is a work in progress. It would be possible to include such a model in the framework presented here, but the simulations shown do not capture all the details of a multipass build in which a series of phase transformations have taken place.

The SCA model, though faster than equivalent FEM models, is still limited in the number of grains it can capture by the computational complexity of the CP model. Very large deformation predictions may be inaccurate, since grain boundary motion is not captured and other relatively more complex modes are discounted. Furthermore, even though the grain geometry used is that of the β phase, mechanical properties of the α phase (hcp) are used to more realistically capture mechanical behavior. This may be a reasonable approximation, and could easily be corrected if a model for solid state phase transformation is introduced.

3.6.2. Outlook for the framework

We claim the framework demonstrated here is sufficiently general to include macroscale simulations, if needed, or any other related module required. We show the addition of a CA model as an example of this. However, one could envisage the addition of further hubs. One option would be a design hub, which might include modules for CAD/CAE tools, slicing and machine control, and/or topological optimization. Another possible hub might implement models to capture post-processing steps such as HIP, heat and/or chemical treatment, and surface finishing.

4. Conclusion

We have demonstrated a process–structure–properties prediction framework for additive manufacturing that connects models for each aforementioned stage and requires only basic material properties and processing conditions. The framework provides a means to capture AM process that is extensible and flexible: additional models could be included (e.g. post-processing), and different types of analysis could be considered (e.g. continuum scale). This is enabled by a simple database format used to transport material state information between computational modules. Using this framework, we have shown a sample computation: a comparison between hatch spacings in SEBM Ti–6Al–4V, with all other process parameters held constant. The decrease in fatigue life that results from lack-of-fusion porosity occurring at too large a spacing was demonstrated, consistent with experimental results. We have thereby shown that this framework enables computational design of the AM process, at least within the constraints of model applicability, using parameters derived from AM machines, raw powder, and studies of wrought material. Frameworks such as this can be expanded upon and developed to be practically useful tools.

Acknowledgments

G. J. Wagner and W.K. Liu acknowledge the support by the National Science Foundation (NSF) Cyber–Physical Systems (CPS) under Grant No. CPS/CMMI-1646592. W. Liu, C. Yu, W. Yan and Y. Lian acknowledge the support by the Center for Hierarchical Materials Design (CHiMaD) under Niational Institute of Standards and Technology (NIST) Grant No. 70NANB14H012. O.L. Kafka acknowledges the support of the National Science Foundation Graduate Research Fellowship under Grant No. DGE-1324585.

References

[1] M. Jamshidinia, F. Kong, R. Kovacevic, Numerical modeling of heat distribution in the electron beam melting® of Ti-6Al-4V, J. Manuf. Sci. Eng. 135 (6) (2013) 061010.
[2] I. Roberts, C. Wang, R. Esterlein, M. Stanford, D. Mynors, A three-dimensional finite element analysis of the temperature field during laser melting of metal powders in additive layer manufacturing, Int. J. Mach. Tools Manuf. 49 (12) (2009) 916–923.
[3] W. Yan, W. Ge, J. Smith, G. Wagner, F. Lin, W.K. Liu, Towards high-quality selective beam melting technologies: modleing and experiments of single track formations, in: 26th Annual International Symposium on Solid Freeform Fabrication, Austin, Texas, 2015.
[4] C. Körner, A. Bauereiß, E. Attar, Fundamental consolidation mechanisms during selective beam melting of powders, Modelling Simul. Mater. Sci. Eng. 21 (8) (2013) 085011.
[5] C. Qiu, C. Panwisawas, M. Ward, H.C. Basoalto, J.W. Brooks, M.M. Attallah, On the role of melt flow into the surface structure and porosity development during selective laser melting, Acta Mater. 96 (2015) 72–79.
[6] W. Yan, W. Ge, Y. Qian, S. Lin, B. Zhou, W.K. Liu, F. Lin, G.J. Wagner, Multi-physics modeling of single/multiple-track defect mechanisms in electron beam selective melting, Acta Mater. 134 (2017) 324–333.
[7] S.A. Khairallah, A. Anderson, Mesoscopic simulation model of selective laser melting of stainless steel powder, J. Mater Process. Technol. 214 (11) (2014) 2627–2636.
[8] S. Ghosh, J. Choi, Three-dimensional transient finite element analysis for residual stresses in the laser aided direct metal/material deposition process, J. Laser Appl. 17 (3) (2005) 144–158.
[9] L. Parry, I. Ashcroft, R. Wildman, Understanding the effect of laser scan strategy on residual stress in selective laser melting through thermo-mechanical simulation, Addit. Manuf. 12 (2016) 1–15.

[10] J. Heigel, P. Michaleris, E. Reutzel, Thermo-mechanical model development and validation of directed energy deposition additive manufacturing of Ti-6Al-4V, Addit. Manuf. 5 (2015) 9–19.
[11] N. Hodge, R. Ferencz, J. Solberg, Implementation of a thermomechanical model for the simulation of selective laser melting, Comput. Mech. 54 (1) (2014) 33–51.
[12] S. Leuders, M. Vollmer, F. Brenne, T. Tröster, T. Niendorf, Fatigue strength prediction for titanium alloy TiAl6V4 manufactured by selective laser melting, Metall. Mater. Trans. A 46 (9) (2015) 3816–3823.
[13] R. Hedayati, H. Hosseini-Toudeshky, M. Sadighi, M. Mohammadi-Aghdam, A. Zadpoor, Computational prediction of the fatigue behavior of additively manufactured porous metallic biomaterials, Int. J. Fatigue 84 (2016) 67–79.
[14] B. Schoinochoritis, D. Chantzis, K. Salonitis, Simulation of metallic powder bed additive manufacturing processes with the finite element method: A critical review, Proc. Inst. Mech. Eng. Part B: J. Eng. Manuf. 23 (1) (2015) 96–117.
[15] M. Markl, C. Körner, Multiscale modeling of powder bed–based additive manufacturing, Annu. Rev. Mater. Res. 46 (2016) 93–123.
[16] M. Francois, A. Sun, W. King, N. Henson, D. Tourret, C. Bronkhorst, N. Carlson, C. Newman, T. Haut, J. Bakosi, J. Gibbs, V. Livescu, S.V. Wiel, A. Clarke, M. Schraad, T. Blacker, H. Lim, T. Rodgers, S. Owen, F. Abdeljawad, J. Madison, A. Anderson, J.-L. Fattebert, R. Ferencz, N. Hodge, S. Khairallah, O. Walton, Modeling of additive manufacturing processes for metals: Challenges and opportunities, Curr. Opin. Solid State Mater. Sci. 21 (4) (2017) 198–206.
[17] P.C. Collins, C.V. Haden, I. Ghamarian, B.J. Hayes, T. Ales, G. Penso, V. Dixit, G. Harlow, Progress toward an integration of process–structure–property–performance models for "three-dimensional (3-D) printing" of titanium alloys, JOM 66 (7) (2014) 1299–1309.
[18] J. Smith, W. Xiong, W. Yan, S. Lin, P. Cheng, O.L. Kafka, G.J. Wagner, J. Cao, W.K. Liu, Linking process, structure, property, and performance for metal-based additive manufacturing: computational approaches with experimental support, Comput. Mech. 57 (2016) 583–610.
[19] W. Yan, S. Lin, O.L. Kafka, C. Yu, Z. Liu, Y. Lian, S. Wolff, J. Cao, G.J. Wagner, W.K. Liu, Modeling process-structure-property relationships for additive manufacturing, Front. Mech. Eng. (2018) 1–11.
[20] W. Yan, S. Lin, O.L. Kafka, Y. Lian, C. Yu, Z. Liu, J. Yan, S. Wolff, H. Wu, E. Ndip-Agbor, et al., Data-driven multi-scale multi-physics models to derive process–structure–property relationships for additive manufacturing, Comput. Mech. (2018) 1–21.
[21] J. Smith, W. Xiong, J. Cao, W.K. Liu, Thermodynamically consistent microstructure prediction of additively manufactured materials, Comput. Mech. 57 (2016) 359–370.
[22] S. Ghosh, J. Choi, Modeling and experimental verification of transient/residual stresses and microstructure formation in multi-layer laser aided DMD process, J. Heat Transfer 128 (7) (2006) 662–679.
[23] T.M. Rodgers, J.D. Madison, V. Tikare, Simulation of metal additive manufacturing microstructures using kinetic Monte Carlo, Comput. Mater. Sci. 135 (2017) 78–89.
[24] W. Tan, Y.C. Shin, Multi-scale modeling of solidification and microstructure development in laser keyhole welding process for austenitic stainless steel, Comput. Mater. Sci. 98 (2015) 446–458.
[25] S.A. Khairallah, A.T. Anderson, A. Rubenchik, W.E. King, Laser powder-bed fusion additive manufacturing: Physics of complex melt flow and formation mechanisms of pores, spatter, and denudation zones, Acta Mater. 108 (2016) 36–45.
[26] W. Yan, Y. Qian, W. Ge, S. Lin, W.K. Liu, F. Lin, G.J. Wagner, Meso-scale modeling of multiple-layer fabrication process in selective electron beam melting: inter-layer/track voids formation, Mater. Des. 141 (2018) 210–219.
[27] W. Yan, J. Smith, W. Ge, F. Lin, W.K. Liu, Multiscale modeling of electron beam and substrate interaction: a new heat source model, Comput. Mech. 56 (2) (2015) 265–276.
[28] W. Yan, W. Ge, J. Smith, S. Lin, O.L. Kafka, F. Lin, W.K. Liu, Multi-scale modeling of electron beam melting of functionally graded materials, Acta Mater. 115 (2016) 403–412.
[29] C. Gandin, M. Rappaz, A 3D Cellular Automaton algorithm for the prediction of dendritic grain growth, Acta Mater. 45 (5) (1997) 2187–2195.
[30] Y. Lian, S. Lin, W. Yan, W.K. Liu, G.J. Wagner, A parallelized three-dimensional cellular automaton model for grain growth during additive manufacturing, Comput. Mech. (2018) 1–16.
[31] Y.P. Lian, W. Yan, O.L. Kafka, W.K. Liu, G.J. Wagner, Microstructural evolution in selective electron beam melting fabricated Ti-6Al-4V, in preparation.
[32] W. Kurz, B. Giovanola, R. Trivedi, Theory of microstructural development during rapid solidification, Acta Metall. 34 (5) (1986) 823–830.
[33] A.R.A. Dezfoli, W.-S. Hwang, W.-C. Huang, T.-W. Tsai, Determination and controlling of grain structure of metals after laser incidence: Theoretical approach, Sci. Rep. 7 (2017) 41527.
[34] Z. Liu, M. Bessa, W.K. Liu, Self-consistent clustering analysis: An efficient multi-scale scheme for inelastic heterogeneous materials, Comput. Methods Appl. Mech. Engrg. 306 (2016) 319–341.
[35] Z. Liu, M. Fleming, W.K. Liu, Microstructural material database for self-consistent clustering analysis of elastoplastic strain softening materials, Comput. Methods Appl. Mech. Engrg. 330 (2018) 547–577.
[36] T. Belytschko, W.K. Liu, B. Moran, K. Elkhodary, Nonlinear Finite Elements for Continua and Structures, John Wiley & Sons, 2013.
[37] J.A. Moore, D. Frankel, R. Prasannavenkatesan, A.G. Domel, G.B. Olson, W.K. Liu, A crystal plasticity-based study of the relationship between microstructure and ultra-high-cycle fatigue life in nickel titanium alloys, Int. J. Fatigue 91 (2016) 183–194.
[38] S. Al-Bermani, M. Blackmore, W. Zhang, I. Todd, The origin of microstructural diversity, texture, and mechanical properties in electron beam melted Ti-6Al-4V, Metall. Mater. Trans. A 41 (13) (2010) 3422–3434.
[39] J. Thomas, M. Groeber, S. Ghosh, Image-based crystal plasticity FE framework for microstructure dependent properties of Ti-6Al-4V alloys, Mater. Sci. Eng. A 553 (2012) 164–175.
[40] E. Kröner, Statistical Continuum Mechanics, Vol. 92, Springer, 1972.
[41] Z. Liu, O.L. Kafka, C. Yu, W.K. Liu, Data-driven self-consistent clustering analysis of heterogeneous materials with crystal plasticity, in: Advances in Computational Plasticity, Springer, 2018, pp. 221–242.

[42] A. Fatemi, D.F. Socie, A critical plane approach to multiaxial fatigue damage including out-of-phase loading, Fatigue Fract. Eng. Mater. Struct. 11 (3) (1988) 149–165.
[43] M. Shenoy, J. Zhang, D. McDowell, Estimating fatigue sensitivity to polycrystalline Ni-base superalloy microstructures using a computational approach, Fatigue Fract. Eng. Mater. Struct. 30 (10) (2007) 889–904.
[44] M. Janeček, F. Nový, P. Harcuba, J. Stráský, L. Trško, M. Mhaede, L. Wagner, The very high cycle fatigue behaviour of Ti-6Al-4V Alloy, Acta Phys. Polon. A 128 (4) (2015).
[45] Y. Li, D. Gu, Parametric analysis of thermal behavior during selective laser melting additive manufacturing of aluminum alloy powder, Mater. Des. 63 (2014) 856–867.
[46] S. Tammas-Williams, H. Zhao, F. Léonard, F. Derguti, I. Todd, P. Prangnell, XCT analysis of the influence of melt strategies on defect population in Ti-6Al-4V components manufactured by Selective Electron Beam Melting, Mater. Charact. 102 (2015) 47–61.
[47] A. Antonysamy, J. Meyer, P. Prangnell, Effect of build geometry on the -grain structure and texture in additive manufacture of Ti-6Al-4V by selective electron beam melting, Mater. Charact. 84 (2013) 153–168.
[48] P. Li, D. Warner, A. Fatemi, N. Phan, On the fatigue performance of additively manufactured Ti-6Al-4V to enable rapid qualification for aerospace applications, in: 57th AIAA/ASCE/AHS/ASC Structures, Structural Dynamics, and Materials Conference, 2016, p. 1656.
[49] H. Gong, K. Rafi, T. Starr, B. Stucker, Effect of defects on fatigue tests of as-built Ti-6Al-4V parts fabricated by selective laser melting, in: Solid Freeform Fabrication Symposium, University of Texas Austin, Texas, 2012, pp. 499–506.